Effect of spraying parameters on the microstructural and corrosion properties of HVAF-sprayed Fe–Cr–Ni–B–C coatings

A. Milanti [a,*], V. Matikainen [a], H. Koivuluoto [a], G. Bolelli [b], L. Lusvarghi [b], P. Vuoristo [a]

[a] Department of Materials Science, Tampere University of Technology, Korkeakoulunkatu 6, 33720 Tampere, Finland
[b] Department of Engineering "Enzo Ferrari", University of Modena and Reggio Emilia, Via Pietro Vivarelli, 10, 41125 Modena, Italy

A B S T R A C T

Thermally sprayed Fe-based coatings have been extensively studied as future solution in order to replace more expensive, harmful and environmentally dangerous Ni- and WC-based coatings for several industrial applications where high corrosion and wear resistance are required. The aim of the present study is to investigate the effect of spraying parameters on the microstructure and the corrosion resistance of Fe-based coatings manufactured with the High Velocity Air Fuel (HVAF) thermal spray process. Six sets of thermal spraying parameters have been chosen and their effect on the overall quality of coatings was investigated. All HVAF coatings showed comparably dense microstructure with near-zero oxidation, proving the high quality of the deposition process. However, higher anti-corrosion and mechanical properties were achieved by increasing the spraying air pressure and decreasing the particle feeding rate without altering the thickness and the overall deposition rate. Powder feeding rate was reported to have a remarkable effect on microstructure and corrosion properties. Coatings with beneficial compressive residual stresses were successfully obtained by increasing air pressure during spraying which resulted in improved microstructural and corrosion properties.

© 2015 Elsevier B.V. All rights reserved.

1. Introduction

Thermal spraying is a widely spread coating technology process employed in several industrial applications. It consists of molten, semi-molten or solid particles accelerated by a high speed stream of gases towards a substrate in order to form a thick coating [1]. Increasing the deposition efficiency and lowering the costs of the process while preserving the overall high coating quality are the general trends of thermal spraying, in order to reduce the production costs and decrease the environmental impact. Among different solutions, iron-based coatings deposited with thermal spray processes seem to gain growing interest in the research community due to their unique combination of low price, health safety and good mechanical properties [2–4]. Iron-based thermal spray powders generally combine hard precipitates such as borides and carbides in an austenitic and/or ferritic matrix with high chromium content.

High chromium content is designed in order to provide chromium for hard precipitates and on the other hand to provide chromium dissolved in the austenitic solid solution matrix in order to increase the ability to form a thin protective oxide layer. Such design is meant to increase the corrosion resistance of the alloy without altering the

mechanical properties [5]. Moreover, Fe-based coatings have been studied as alternative solution to replace more expensive, harmful and environmentally dangerous Ni- and WC-based coatings for several industrial applications where high corrosion and wear resistance are required. Ni- and WC-based materials have been lately pointed out as potential lung disease and carcinogenic agents and responsible of skin diseases (eczema, allergen), asthma and pneumoconiosis [6,7].

Traditional thermal spray processes like Arc Spraying (AS), Flame Spraying (FS) and Atmospheric Plasma Spraying (APS) have been employed for Fe-based powder deposition [8–13]. However, the high gas temperature, low particle velocity and the lack of a proper shrouding atmosphere of AS, FS and APS processes resulted in large amount of molten particles with a non-uniform heating and solidification, which is detrimental to the overall quality of the coatings. This leads to low hardness, high oxide and porosity content up to 10% which in turn barely offers good protection against aggressive solution to penetrate towards the substrate [8–13]. The High Velocity Oxygen Fuel (HVOF) spray process has also been extensively used for Fe-based coatings due to its ability of depositing dense coatings with high adhesion strength [14–17]. In HVOF spraying, powders are accelerated by the supersonic jet achieved by expansion of the combustion products between oxygen and fuel gases through a convergent–divergent nozzle. Some drawbacks are related to oxidation, to the possible generation of tensile residual stresses [18,19] (whereas compressive residual stresses are preferred in coatings) and, sometimes, thermal deterioration due to the relatively high temperature [3, 20].

* Corresponding author.
  E-mail addresses: andrea.milanti@tut.fi (A. Milanti), ville.matikainen@tut.fi
(V. Matikainen), heli.koivuluoto@tut.fi (H. Koivuluoto), giovanni.bolelli@unimore.it
(G. Bolelli), luca.lusvarghi@unimore.it (L. Lusvarghi), petri.vuoristo@tut.fi (P. Vuoristo).

Recently, High Velocity Air Fuel (HVAF) spraying has been considered as alternative process deposition for Fe-based powders in order to overcome the above mentioned limitations of HVOF. It reduces the cost of operation by replacing pure oxygen with compressed air and it increases the flexibility of high velocity combustion spray processes while retaining their ability to produce high quality coatings [21, 22]. Supersonic jet in HVAF is achieved by combustion of air and fuel gases and subsequent expansion of combustion products through a convergent–divergent nozzle. In M3 HVAF torch, secondary air and fuel mixture is injected at the throat of the secondary nozzle in order to provide additional heat to the process. The M3 torch design (Fig. 1) together with high pressure capabilities and total replacement of oxygen with air assures higher particle velocities, higher powder feeding rate, lower temperature and less oxidizing atmosphere [23,24] resulting in a promising alternative method to manufacture high quality coatings [25–28]. Low oxide content, high retention of powder microstructure, low porosity with an excellent wear and corrosion behaviour were reported in the recent studies of HVAF-sprayed Fe-based coatings [25]. Furthermore, equal or even better wear and corrosion resistance of HVAF-sprayed cermet coatings compared with HVOF-sprayed ones were reported [29]. Moreover, HVAF process has been lately employed for the deposition of amorphous Fe-based coatings with good resistance to sliding and abrasive wear, low friction coefficients and superior corrosion resistance [3, 26]. The HVAF process, which relies more on kinetic energy than on thermal energy, indeed allows minimal microstructural and chemical changes to the complex composition of Fe-based feedstock powders with high Glass Forming Ability (GFA) leading to high amorphous contents in the resulting Fe-based coatings.

Although promising results were obtained with the HVAF process using the latest M3 torch model for the deposition of hard metal powder [30], no study on the effect of spraying parameters of such HVAF process on microstructure and corrosion properties of Fe-based coatings has been performed yet. The present work focuses on the effect of spraying parameters (air/propane pressure ratio in combustion chamber, propane pressure in the convergent–divergent nozzle and the powder feeding rate) on the microstructural and the corrosion properties of HVAF Fe–Cr–Ni–B–C coatings. Structural details were studied by means of scanning electron microscopy (SEM), electrochemical impedance spectroscopy (EIS) and residual stress analysis indicating good correlation with corrosion behaviour of coatings. Corrosion properties were studied with open-circuit potential and polarization measurements.

2. Experimental procedure

2.1. Materials and coating manufacturing

Commercial gas-atomized Fe-based powder Fe–31Cr–12Ni–3.6B–0.6C (wt.%) with nominal size of $-40 + 20$ μm traded as Durmat 512.021 (Durum Verschleiss-Schutz GmbH, Krefeld, Germany), was used as feedstock material. More details of the powder are presented in our previous study [25]. The powder was sprayed onto low carbon steel (Fe52) by Supersonic Air Fuel HVAF (SAF, 3rd generation) M3 (Uniquecoat Technologies LLC, Oilville, VA, USA) spray gun. The sample substrates were attached by screws to a sample holder before spraying, and compressed air was used as cooling medium. Propane was used as main combustion fuel gas (fuel 1) and as well as secondary combustion gas (fuel 2, additional combustion gas inserted into the nozzle, Fig. 1) in order to increase the heat provided to particles. Six sets (1–6) of spraying parameters (Table 1) were studied. Substrates were grit-blasted (Al_2O_3 grits, 36 mesh) prior to the spraying. The process gases are pressure-controlled which also means that the real gas flow rates in the equipment are unknown.

The heat of combustion was varied by selecting three different air–propane pressure ratios (110/106, 116/106 and 120/108) whereas secondary propane gas was regulated at 3 pressures: 108 (0.74), 110 (0.76) and 112 (0.77) psi (MPa). The value of 108 psi (0.74 MPa) was associated to the lowest air–propane ratio (110/106), 110 psi (0.76 MPa) was used for the air–propane ratio of 116/106 and 112 psi (0.77 MPa) for the largest air–propane ratio (120/108). Traverse speed (0.5 m/s), step size (4 mm), stand-off distance (300 mm) of gun and the nitrogen carrier gas flow rate (60 l/min) were kept as constant. The powder feeding rate was varied as 75 g/min and 140 g/min. The number of gun passes was 6 and 4 for the coating samples with powder feeding rate of 75 g/min and 140 g/min, respectively. The sole purpose was to keep the coating thickness approximately at the same level for all coatings.

2.2. Microstructural and mechanical studies

The microstructure of the coatings was investigated by Scanning Electron Microscope (SEM, Philips XL30, The Netherlands) equipped with Energy Dispersive X-ray (EDX) microanalysis whereas phase composition was assessed by X-Ray Diffractometry (XRD, Empyrean, PANAnalytical, The Netherlands, Co-Kα radiation). Experimental conditions include 2θ range 20°–120°, step size 0.02°, beam mask 20 mm, programmable divergent slit fixed at 1/2 degree, Fe-filter and PANAnalytical PIXcel 3D detector. Phase identification was performed using the PANAnalytical X'Pert High Score Plus software using the ICDD JCPDF-2 database (International Centre for Diffraction Data, Newtown Square, PA, USA).

X-ray diffraction was also employed to analyse the surface of the samples after corrosion test (Open-circuit potential measurements (OCP)) in grazing incidence X-ray diffraction mode (GID) (XRD, Empyrean, PANAnalytical, The Netherlands, Co-Kα radiation). GID consists of fixing the incidence angle of the X-ray beam (conventionally designated as ω) to a small value in order to limit the penetration of X-ray through the sample and eventually study the formation of thin outer corrosion layers. Experimental conditions include incidence angle ω = 2°, 2θ range 5°–70°, step size 0.02°, beam mask 15 mm, programmable divergent slit fixed at 1/16 degree, Fe-filter and PANAnalytical PIXcel 3D detector. Phase identification was again performed using the PANAnalytical X'Pert High Score Plus software using the ICDD JCPDF-2 database.
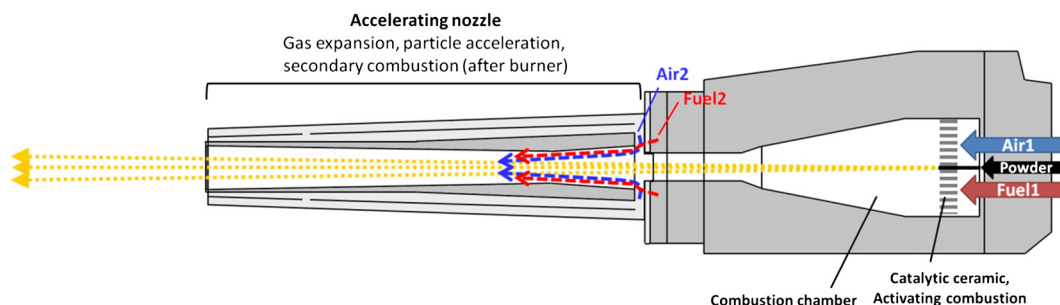

Fig. 1. Schematic representation of HVAF torch.

Table 1
HVAF spray parameters. Traverse speed (0.5 m/s), step size (4 mm), stand-off distance (300 mm) of gun and the nitrogen carrier gas (60 l/min) were kept as constant.

Set	Air pressure, psi (MPa)	Propane gas 1 pressure, psi (MPa)	Propane gas 2 pressure, psi (MPa)	Air–propane 1 pressure ratio	Powder feeding rate (g/min)	Number of passes
1	110 (0.76)	106 (0.73)	108 (0.74)	1.04	75	6
2	110 (0.76)	106 (0.73)	108 (0.74)	1.04	140	4
3	116 (0.80)	106 (0.73)	110 (0.76)	1.09	75	6
4	116 (0.80)	106 (0.73)	110 (0.76)	1.09	140	4
5	120 (0.83)	108 (0.74)	112 (0.77)	1.11	75	6
6	120 (0.83)	108 (0.74)	112 (0.77)	1.11	140	4

Coating thickness was calculated as an average of 10 measurements on SEM images taken on polished cross-sections, prepared by grinding samples embedded in resin with SiC papers up to 4000 mesh and polished with colloidal silica suspension. Coating roughness (R_a) was calculated through 3D optical profilometry (Veeco, WYKO NT1100, USA) in order to get an indirect estimation of particle melting during deposition. Indeed, higher particle melting and velocity generally result in higher particle softening and plastic deformation and in turn particle flattening ratio during deposition leading to lower roughness [31]. The microhardness of HVAF-sprayed coatings was calculated as an average of 20 Vickers microhardness indentations ($HV_{0.3}$) on the polished cross-sections by means of standard microindenter (Matsuzawa MMT-X7, Japan — 300 g normal load).

Residual stresses were characterised by X-ray residual stress analysis, using the ω-tilt method, on as-sprayed samples and on samples polished up to mirror-like surface finish. Mechanical removal of material in grinding and polishing may alter the actual stress state of the coatings [32]. However, Co Kα radiation with large X-ray penetration allowed an average residual stress calculation over large coating thickness making any possible superficial alteration not significant. Line focus configuration with beam mask 20 mm and programmable divergent slit fixed at 1/2 degree with the Euler cradle stage was used. 7 symmetric ψ tilt values were employed corresponding to $\sin^2\psi = 0$; 0.1; 0.2; 0.3, along three directions corresponding to $\varphi = 0°$, $\varphi = 45°$ and $\varphi = 90°$. The (3 1 1) peak of austenite, located at $2\theta = 110.95°$, was acquired by scanning a 2θ range of 7°, and the deformation in the (h k l) = (3 1 1) direction was determined by Eq. (1)

$$\varepsilon_\psi = (d_\psi - d_0)/d_0 \tag{1}$$

where d_ψ is the lattice spacing measured at ψ tilt and d_0 the unstressed lattice spacing. Data were interpreted by implementing the $\sin^2\psi$ method according to the formulation described in [32], in the hypothesis of plane stress condition. The relations for directions corresponding to $\varphi = 0°$, $\varphi = 45°$ and $\phi = 90°$ Eqs. (2)–(4) are the following:

$$\varepsilon_{\psi,\varphi=0°}^{hkl} = \frac{1}{2}S_2^{hkl}\sigma_x\sin^2\psi + S_1^{hkl}(\sigma_x + \sigma_y) \tag{2}$$

$$\varepsilon_{\psi,\varphi=45°}^{hkl} = \frac{1}{2}S_2^{hkl}\left(\frac{\sigma_x + \sigma_y}{2} + \tau_{xy}\right)\sin^2\psi + S_1^{hkl}(\sigma_x + \sigma_y) \tag{3}$$

$$\varepsilon_{\psi,\varphi=90°}^{hkl} = \frac{1}{2}S_2^{hkl}(\sigma_y)\sin^2\psi + S_1^{hkl}(\sigma_x + \sigma_y). \tag{4}$$

The values of the X-ray elastic constants employed for equations were taken from [33] for the (3 1 1) peak of austenite: $(1/2)S_2 = 7.52 * 10^{-6}$ mm²/N; $S_1 = -1.80 * 10^{-6}$ mm²/N.

It is worth noting that unstressed lattice spacing d_0 is not known a priori, so the strains were first calculated from an initial assumption $d_0 \approx d_{\varphi,\psi=0°}$. Despite the assumption $d_0 \approx d_{\varphi,\psi=0}$, the slopes of $\varepsilon_{\psi\phi}$ vs. $\sin^2\psi$ fitting depicted in Eqs. (2), (3) and (4) are numerically correct. Therefore, σ_x, σ_y and τ_{xy} were first calculated through the slopes of

Eqs. (2), (3) and (4). Afterwards, σ_x and σ_y values were used for calculating a new unstressed planar distance d_0 value (Eq. (5) obtained from Eqs. (1) and (2) by imposing ψ equals 0).

$$\frac{d_{\varphi,\psi=0°}^{hkl} - d_0^{hkl}}{d_0^{hkl}} = \varepsilon_{\varphi,\psi=0°}^{hkl} = S_1^{hkl}(\sigma_x + \sigma_y) \rightarrow d_0^{hkl} = \frac{d_{\varphi,\psi=0°}^{hkl}}{1 + S_1^{hkl}(\sigma_x + \sigma_y)} \tag{5}$$

Strains and σ_x, σ_y and τ_{xy} were therefore iteratively recalculated (MatLab code employed) until convergence is reached.

2.3. Corrosion studies

The corrosion behaviour of HVAF-sprayed coatings was evaluated with open-circuit potential measurements (OCP) and potentiodynamic polarization technique. All samples were ground and polished to Ra ≈ 0.02 μm before testing in order to remove any influence from the original surface roughness and from possible defects in the top layer of the coating (as shown later in Section 3.1). OCP measurements were performed by glueing a plastic tube (diameter 20 mm) to the coating surface. An amount of 12 ml of a 3.5 wt.% NaCl aqueous solution was filled into the tube. The open-circuit potential was measured up to 24 days of immersion (reference electrode (Ag/AgCl/KCl(sat))) and afterwards exposed surface of coatings was observed by means of stereomicroscopy. Potentiodynamic polarization technique was performed with the standard three-electrode cell with a wide overpotential range (from −0.4 V vs. OC to 1.4 V vs. OC — scan rate 0.5 mV/s) in 0.1 M solution of hydrochloric acid. Corrosion parameters such as corrosion potential (E_{corr}) and corrosion current density (I_{corr}) were calculated by using Gamry Echem Analyst Software. The software was also used for calculations of anodic and cathodic Tafel constants (β_a and β_c) needed for polarization resistance calculations. The polarization resistance (R_P) of coatings was calculated by using the Stern–Geary Eq. (6) [34]:

$$R_P = \beta_a \cdot \beta_c/(2.3 \cdot (\beta_a + \beta_c) \cdot I_{corr}) \tag{6}$$

where β_a and β_c are the slope of anodic and cathodic Tafel line respectively and I_{corr} is the corrosion current density.

In addition, electrochemical impedance spectroscopy (EIS) was employed by using a non-corrosive electrolyte in order to estimate the overall open porosity (interconnected porosity) as described in [35,36] in order to avoid the limitations of image analysis technique. EIS was performed in a three-electrode electrochemical cell where the reference electrode is Ag/AgCl/KCl(sat) and the counter electrode is a platinum grid. The samples were ground and polished as described previously in order to avoid the effects of surface roughness and of defects in the topmost coating layer. The results were represented through Bode plots. The choice of a suitable equivalent circuit with a reliable description of electrochemical processes occurring during the test returns quantitative data (resistance and capacitance values) related to coating open-porosity. The testing conditions were the following: exposed surface 0.95 cm², start frequency 300 kHz, end frequency 1 mHz, voltage perturbation amplitude ± 20 mV around OCP measured for 30 s before EIS measurement. The electrolyte was a 0.01 M $K_3Fe(CN)_6/K_4Fe(CN)_6$ aqueous solution, chosen for its stability and for the high redox reversibility of the $Fe(CN)_6^{3-} + e^- \leftrightarrow Fe(CN)_6^{4-}$ reaction, with an equilibrium potential of about 280 mV vs. (Ag/AgCl/KCl(sat)), as previously described in [37]. Tests were started with a 0.5 h delay to allow full impregnation of the coating by the test solution and complete stabilization of the open-circuit potential.

3. Results and discussions

3.1. Microstructural and mechanical properties of coatings

All HVAF-sprayed coatings showed very dense microstructure (Fig. 2) with particle boundaries barely visible (high magnifications in
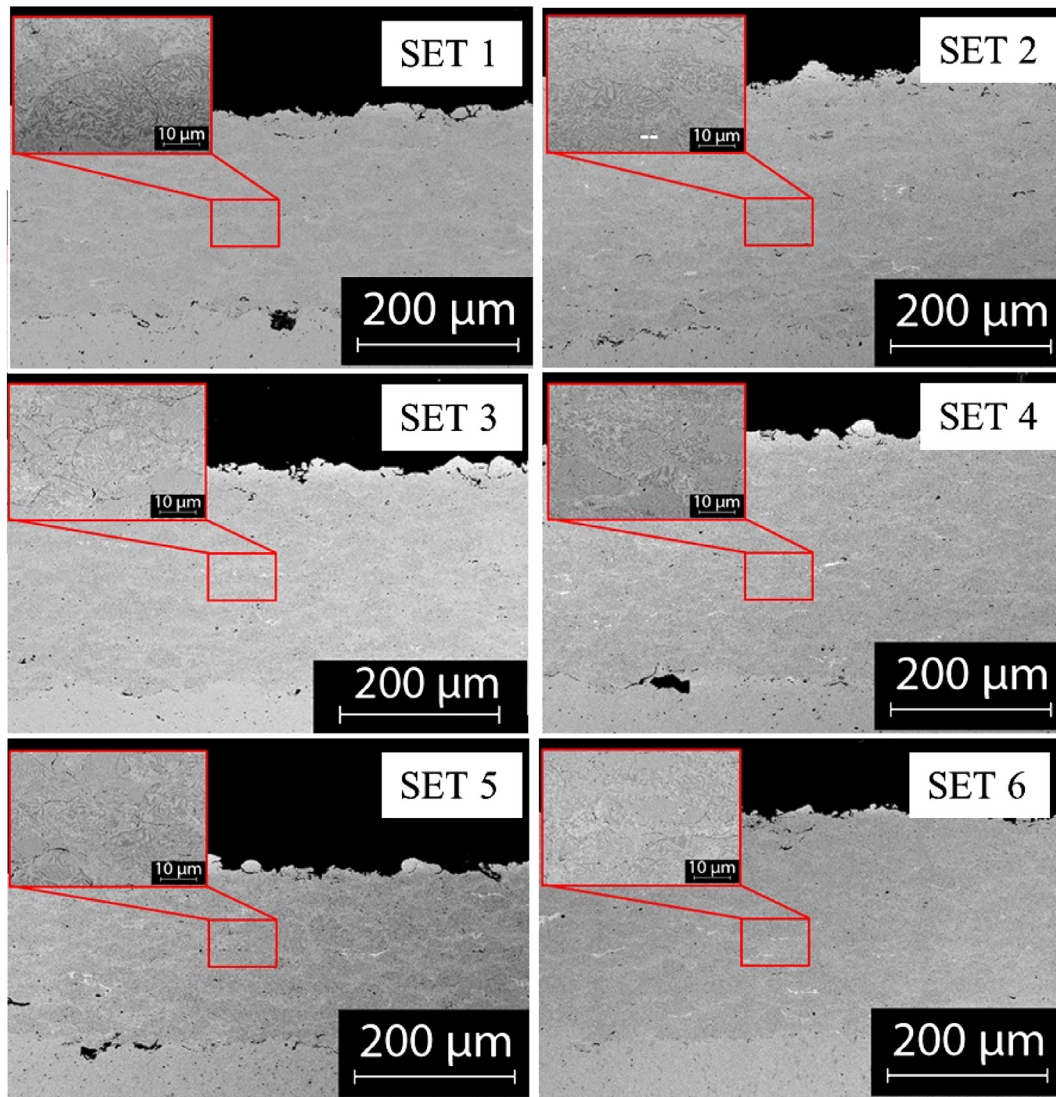
Fig. 2. Cross-sectional structure of HVAF-sprayed Fe-based coatings of SET 1, 2, 3 4, 5 and 6. SEM (BSE) images.

Fig. 2) proving good inter-particle bonding. One can notice that the near-surface region of all coatings has some pores. This has been reported as characteristic of high-kinetic thermal sprayed coatings where the lack of particles hammering (primary role in coating densification [16,32]) in the last layers deposited contributes to create more porous near-surface layers. It is worth saying that generally in practical use the outer porous layer is entirely removed by grinding and polishing coatings before use. However, such external porous layer was reported to be much thinner when compared to the same powder composition sprayed with HVOF in our previous study [16].

Coating thicknesses are presented in Fig. 3 and Table 2. Larger coating thickness and larger thickness per pass (larger deposition rate and deposition efficiency) were measured for samples with higher powder feeding rate (2, 4, 6). The powder feeding rate of samples 2, 4 and 6 is nearly twice as large as those of samples 1, 3 and 5; therefore, one can state that the deposition efficiency of samples sprayed with the same parameters (1/2, 3/4 and 5/6) but with different powder feeding rate is comparable proving the high versatility of the HVAF process. Furthermore, even though the combustion ratio of each parameter setting is not known a priori, by observing the cross-sectional image of the coatings (particle boundaries and particle flattening ratio) it is inferred that increasing air pressure decreases the flame temperature. An increase of air pressure is also thought to raise particle velocity. Kuroda et al. [38] have similarly reported higher particle velocity when dealing with

higher air pressure in HVAF spray process. Having said that, the increase of air pressure (1 < 3 < 5 and 2 < 4 < 6) (Fig. 3) can be resulted in increase of flame velocity and decrease of flame temperature.

Allegedly, when dealing with lower particle feeding rate (75 g/min, samples 1, 3 and 5) a slight increase of air pressure seemed not to
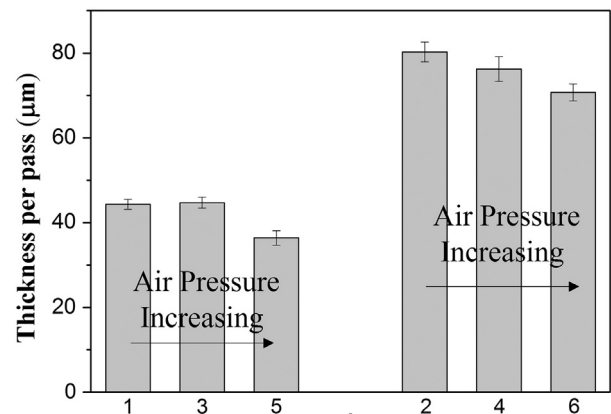

Fig. 3. Thickness of pass of the coatings (grouped according to powder feeding rate — 1, 3, 5 75 g/min and 2, 4, 6 140 g/min).

Table 2
Powder feeding rate **f**, thickness **d**, thickness per pass **d′**, ratio of thickness per pass and powder feeding rate **d′/f**, hardness ($HV_{0.3}$) and roughness R_a of the coatings.

Set	Powder feeding rate f (g/min)	Coating thickness d (μm)	Thickness-pass d′ (μm)	Ratio d′/f	Hardness ($HV_{0.3}$)	Roughness R_a (μm)
1	75	265.9 ± 7.0	44.3 ± 1.2	0.59	732 ± 62	7.5 ± 0.4
2	140	321.1 ± 9.4	80.3 ± 2.4	0.57	753 ± 47	7.3 ± 0.4
3	75	268.5 ± 7.8	44.7 ± 1.3	0.60	781 ± 48	7.5 ± 0.4
4	140	305.6 ± 11.6	76.3 ± 2.9	0.54	733 ± 46	7.2 ± 0.5
5	75	218.4 ± 10.1	36.4 ± 1.7	0.49	735 ± 47	7.3 ± 0.6
6	140	282.8 ± 8.0	70.7 ± 2	0.51	733 ± 41	7.3 ± 0.3

Fig. 5. Equivalent circuit employed for data fitting in EIS measurements.

alter the deposition efficiency (comparable deposition efficiency of samples 1 and 3, Fig. 3). Indeed, as found in the study of Wang et al.[39], lowering the powder feeding rate may increase heat transfer to particles and in turn a slight increase of air pressure may not significantly alter the particle melting and the overall coating deposition process. However, further increase of air pressure led to lower powder deposition (sample 5, Fig. 3) proving the inadequate powder melting (sample 5, Fig. 2, particle boundaries largely visible). Conversely, lower deposition efficiency was reported for any air pressure increase when dealing with higher powder feeding rate (140 g/min, samples 2, 4 and 6) (Fig. 3). Apparently, with high particle feeding rate, increasing the air pressure simultaneously increased the particle velocity and lowered particle temperature, which seems to be disadvantageous for the deposition efficiency.

The microhardness values of HVAF-sprayed coatings ranged from 730 $HV_{0.3}$ to 780 $HV_{0.3}$ but all differences are always comprised within the standard deviations (see Table 2). The lack of visible porosity and the noticeably similar microstructure led to similar coatings hardness except sample 3 whose microhardness appeared to be the highest. Comparable coating roughness was also reported. It is generally presented that higher flame temperature and higher particle velocity lead to higher flattening ratio of particles which in turn results in lower coating roughness [31]. However, no remarkable differences were observed for the studied coatings possibly due to the likely simultaneous decrease of flame temperature and increase of particle velocity when increasing air pressure.

According to XRD patterns (Fig. 4), all coatings seem to retain the powder microstructure proving no undesired reactions occurred at high temperatures, which in turn demonstrates the high reliability of the HVAF spray process in preventing thermal alterations. Phase identification of XRD patterns revealed the presence of large amounts of austenitic (f.c.c.) ϒ matrix (JCPDS 98-010-8132) and several low
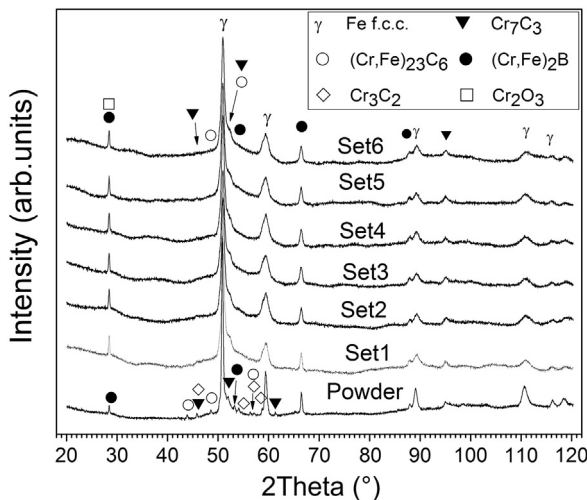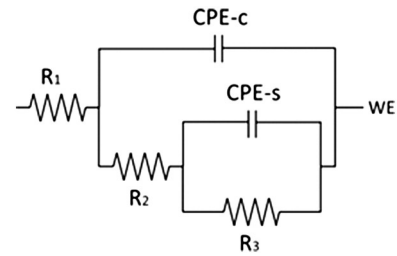
intensity peaks were assigned to chromium and iron mixed boride $(Cr,Fe)_2B$ (JCPDS 01-072-1073) which seems to be the most abundant secondary phase. Other small peaks may be assigned to chromium and iron mixed carbides Cr_3C_2 98-061-7482, Cr_7C_3 01-089-5902, $(Cr,Fe)_{23}C_6$ JCPDS 98-006-2669. Moreover, a small presence of Cr_2O_3 (JCPDS 04-008-6181) is assumed due to the increase of the peak at $2\theta \approx 28°$ and to the low intensity peak at $2\theta \approx 38°$. Although the coatings seem to retain the microstructure of the powder, it is worth noting the slight broadening of the highest intensity peak of austenite ($2\theta \approx 51°$) much likely due to micro-strain or grain size refinement. This could be due to the severe plastic deformation of the particles upon impact, and/or to particle melting and to the subsequent re-solidification of a finer crystalline structure than that of the original feedstock powder.

3.1.1. Electrochemical impedance spectroscopy

EIS measurement was chosen as a method to estimate the overall inter-connecting porosity of the coatings because no visible pores were detected from the cross-sections by image analysis. Indeed, when dealing with dense coatings, image analysis limitations are related to the problem of detecting sub-micron porosity at particles interfaces [37]. Conversely, EIS is a powerful, non-destructive method which relies on small AC-voltage signal (20 mV) and it allows us to evaluate the resistance and capacitance of the coatings through a fit of the data with a proper model circuit. Non-corrosive, highly stable 0.01 M $K_3Fe(CN)_6$/$K_4Fe(CN)_6$ aqueous solution with high redox reversibility was chosen as electrolyte in order to have a reliable open porosity estimation. In the EIS measurement, the model circuit in Fig. 5 was employed as model circuit for the excellent data fitting (goodness of fit $\approx 10^{-6}$) and because it is commonly used in the description of the electrochemical behaviour of thermally sprayed coatings [37].

R_1 represents the resistance of the electrolyte (it is important noting that even though a modern 3-electrode cell was used with a compensation for the solution resistance between the counter and the reference

Fig. 4. XRD patterns of HVAF Fe-based coatings (1–6) and powder.
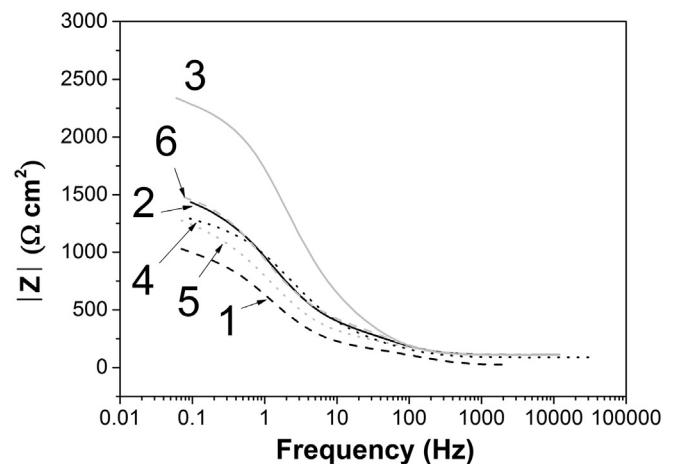
Fig. 6. EIS measurements, Bode plot of tested coatings.

Table 3
EIS test results.

Set	R_1 (Ω)	R_2 (Ω)	C from R_2 and CPE-c (μF)	C from R_3 and CPE-s (μF)	R_3 (Ω)
1	24.7	124.9	11.5	258	1151
2	108.4	243.6	13.1	135	1176
3	106.8	521.7	13.1	45	1748
4	87.32	175.1	12.8	73.7	1089
5	107.4	154.1	12.9	173	1090
6	109.3	301	2.5	166	1148

Note: effective capacitance values C are computed for each (CPE,R) parallel subcircuit using Eq. (8).

electrode, the solution resistance has always to be considered in the model circuit). The parallel subcircuit CPE-c/R_2 describes coating resistance and capacitance. CPE (Y_0,n) is a constant phase element which is generally employed instead of double layer capacitance in real electrochemical processes [35,36], whose impedance is expressed as presented in Eq. (7):

$$Z_{CPE} = 1 / \left[Y_0 (j\omega)^n \right] \qquad (7)$$

where j = the imaginary unit, $\omega = 2\pi f$ and f = the frequency, Y_0 and n = CPE parameters (when n = 1, the CPE becomes an ideal capacitance).

The second parallel subcircuit CPE-s/R_3 describes the double layer capacitance and charge transfer resistance at the electrolyte/working electrode interface. Specifically, R_3 is the charge transfer resistance and it represents the actual double layer current resistance at coating/electrolyte interface. Indeed, the non-corrosive nature of the electrolyte
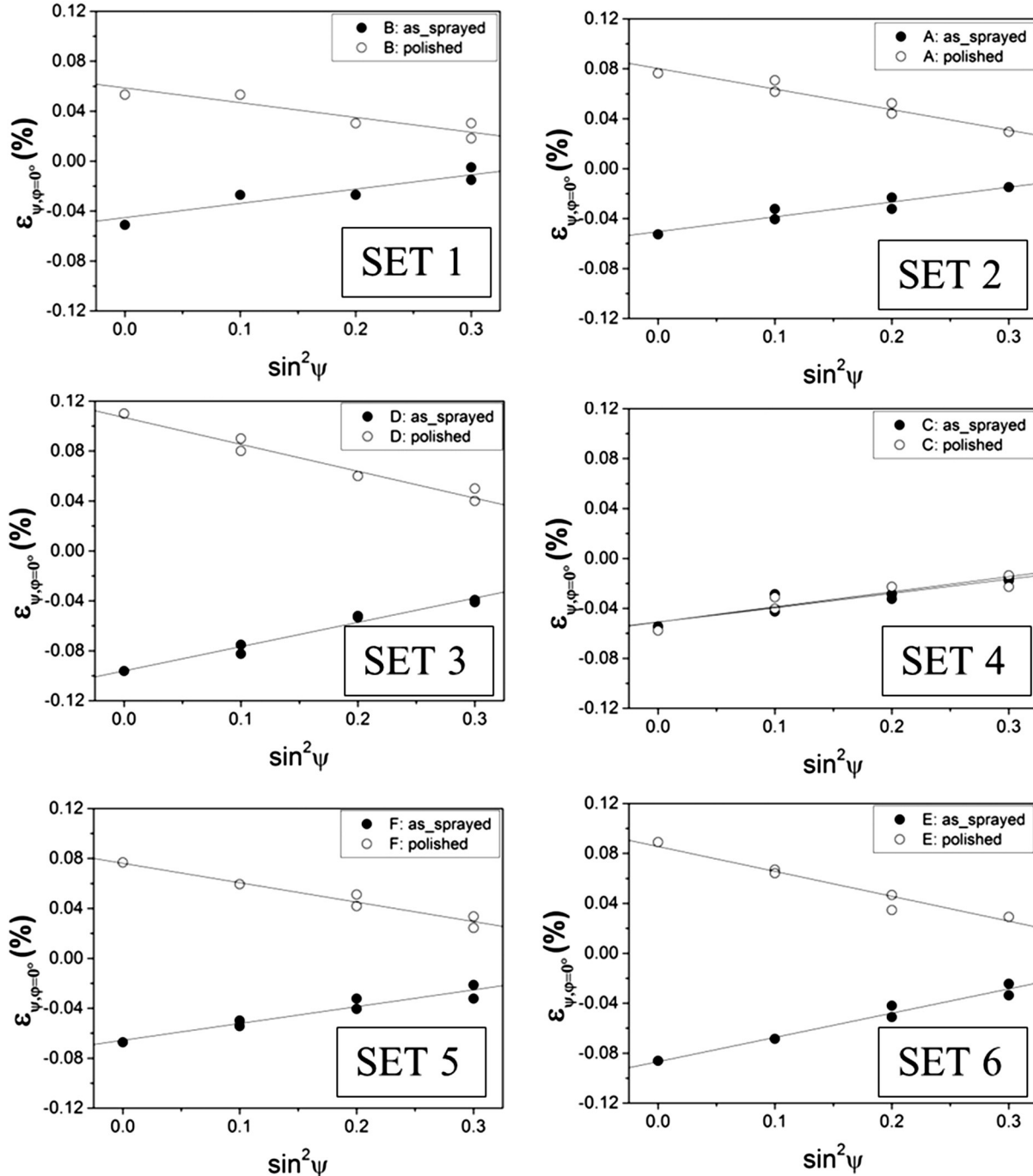

Fig. 7. ε_ψ vs. $\sin^2\psi$ plots along direction $\varphi = 0°$ calculated on as_sprayed and polished coatings of austenite plane (h k l) = (3 1 1).

Table 4
Residual stress calculated by XRD analysis. Values recalculated with optimized value of d_0 unstressed planar distance of austenite plane (h k l) = (3 1 1).

Set		σ_1 (MPa)	σ_2 (MPa)	$\sigma_1 + \sigma_2$ (MPa)	τ_{12} (MPa)
1	As_sprayed	152	131	283	−3
	Polished	−157	−139	−296	−1
2	As_sprayed	158	134	292	14
	Polished	−219	−205	−424	−15
3	As_sprayed	258	276	534	15
	Polished	−277	−327	−604	−10
4	As_sprayed	152	150	302	9
	Polished	161	159	320	−12
5	As_sprayed	179	195	374	−23
	Polished	−207	−220	−427	42
6	As_sprayed	258	220	478	−6
	Polished	−265	−230	−495	−13

provides the electrons and ions needed for the current flow by means of highly reversible and stable redox reaction.

Without performing numerical fitting, it can be immediately noted (Bode plot Fig. 6) that sample 3 showed higher resistant behaviour (the low frequency region is resistive since the impedance of capacitors at low frequency is very high). The Bode plot of sample 3 at low frequency approaches a value of resistance of approximately 2 kΩ which is higher than those of other coatings (between 1 kΩ and 1.5 kΩ). The quantitative electrochemical parameters obtained after fitting through the model circuit (Fig. 4) are shown in Table 3. Specifically, based on electrochemical considerations, it was shown in [40,41] that each subcircuit consisting of a resistance R in parallel with a constant phase element (characterised by the parameters Y_0, n) can be associated to an effective capacitance C according to Eq. (8):

$$C = Y_0^{1/n} R^{(1-n)/n}. \tag{8}$$

Sample 3 possesses higher R_3 proving lower exposed coating/electrolyte interface and therefore lower coating open porosity. Furthermore, sample 3 also possesses the lowest value of effective double layer capacitance (obtained from R_3 and from the Y_0, n parameters of the CPE-s element using Eq. (8), and listed in Table 3). By definition

the capacitance is inversely proportional to the distance between the two conductive plates and directly proportional to the electrical permittivity of the material and to the overall plate area. Since the distance (i.e., the thickness of the electrical double layer formed onto the electrode surface) and the electrical permittivity of the test medium do not change among the various samples, a decrease of the effective double layer capacitance may be attributed to lower electrolyte penetration (i.e., lower overall area) and thus, lower open porosity.

The overall resistance (R_3) of the coatings appeared relatively low because of the reversible redox of the electrolyte. Such redox occurs at approximately 280 mV and the open cell potential (potential at open circuit) of tested coatings is about 260–270 mV. Therefore, during the EIS measurement, the AC-potential oscillated above and below 280 mV making the electrolyte redox extremely fast with a large electron formation leading to high AC-current and relatively low resistance. Therefore, it is important to remark that the low R_3 value is, in this case, not related to low electrochemical corrosion resistance of the coatings, since no corrosion reaction is involved in the present electrochemical process.

3.1.2. Residual stress measurements

In residual stress measurements, a good linear fitting was found for the ε_ψ vs. $\sin^2\psi$ plots of all HVAF Fe-based coatings (Fig. 7). Most of the coatings presented tensile residual stresses in as-sprayed condition and slightly compressive ones when they were polished with fairly low shear stresses. During the deposition two main mechanisms occur in high velocity thermal spray processes: 1) mechanical interlocking of particles due to rapid quenching of molten or semi molten particles which creates tensile stresses at particles boundaries due to the shrinkage of lamellae; and 2) peening effect. In high kinetic energy thermal spray processes, such as HVAF, peening effect is a remarkable mechanism in coating building-up and it relies on the high velocity of solid particles which efficiently hammer the previously deposited coating layers [32]. For such a reason, despite the high penetration of Co radiation which may actually collect information several micrometres deep into the coatings, all as-sprayed HVAF coatings showed tensile residual stresses due to the lack of peening effect on the last deposited coating layer. Instead, compressive residual stresses were reported for polished coatings. It should be noticed that the mechanical polishing may have
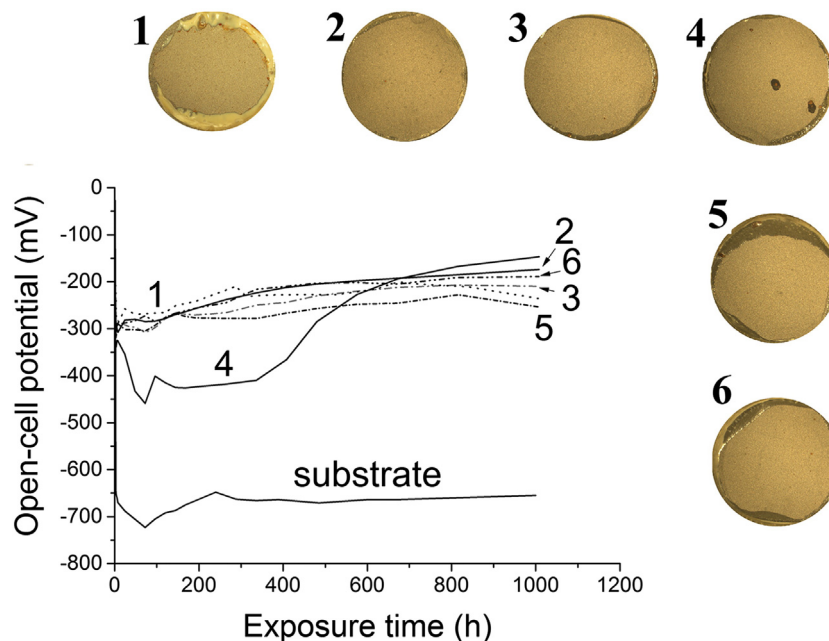
Fig. 8. Open-circuit potential behaviour of the coatings as a function of exposure time in 3.5 wt.% NaCl solution. Ag/AgCl reference electrode. Stereomicroscopy images of coating surfaces after 1000 h exposure are also provided.
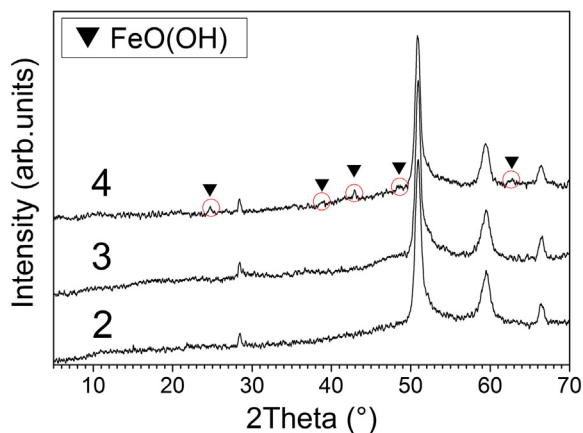
Fig. 9. Grazing Incidence X-ray Diffractometry (GID) patterns of coatings 2, 3 and 4 after 1000 h OCP exposure. (For interpretation of the references to color in this figure, the reader is referred to the web version of this article.)

actually modified the residual stresses of coatings. However, the penetration depth of the Co-Kα radiation in Fe is of more than 10 μm (the attenuation length of the Co-Kα radiation in pure Fe is ≈23 μm at an incidence angle of 80°, as computed from [42]), i.e., it exceeds the depth which would be reasonably expected to bear any polishing-induced alteration. Since the linearity of the ε_ψ vs. $\sin^2\psi$ plots does not suggest any significant through-thickness stress gradient, it is concluded that the stress alterations from polishing in the vicinity of the top surface can be neglected. The only exception was found in sample 4 whose residual stresses in polished condition were reported to be slightly tensile (Table 4). Despite the increase of spraying pressures for set 4, a decrease of temperature may have occurred in deposition conditions which might have provided uneven particle melting. Therefore it can lead to low peening effect so in this case we do not see stresses turning compressive below the surface. Conversely, sample 3 (sprayed with the same spraying pressures of sample 4 but powder feeding rate 75 g/min), showed the largest compressive residual stresses and among the lowest shear residual stresses. It is worth remembering that sample 3 and sample 4 were sprayed with the same spraying parameters but with different powder feeding rate (75 g/min for sample 3 and 140 g/min for sample 4). Thus, it can be stated that the powder feeding rate has noticeable importance on melting and peening effects during the HVAF spray process. A possible explanation might be found in the higher specific heat provided to particles if powder feeding rate is lowered [39]. The same spraying parameters for sample 3 (75 g/min) and sample 4 (140 g/min) led to totally different

residual stress state much likely due to higher and more even heat provided to particles while spraying sample 3 (more even particle softening and/or melting). Furthermore, high compressive residual stress seemed to play an important role on coating hardness. Indeed, compressive residual stresses tend to counteract the penetration of the indenter resulting in lower penetration and high microhardness (sample 3 simultaneously exhibits the highest microhardness, Table 2, and the highest compressive residual stresses, Table 4).

3.2. Corrosion properties

3.2.1. Open-circuit potential behaviour

Through-porosity (open-porosity) was evaluated by open-circuit potential (OCP) measurements up to 24 days immersion. Coating top-surface was evaluated after immersion by stereomicroscopy in order to estimate the penetration of the electrolyte through the coating towards the substrate. Furthermore, grazing incidence X-ray diffraction (GID) was carried out to determine the possible formation of detrimental and voluminous corrosion products at the coating surface.

At the very early stage of the test, coatings 1, 2, 3, 5 and 6 reported high potential, which slowly increased throughout the test. Conversely, coating 4 steadily decreased its potential within the first 100 h towards the characteristic value of the substrate, proving the penetration of the electrolyte through open porosity or localized defectiveness. However, after such a quick drop, its potential increased to higher values probably due to clogging of open-porosity rather than passivation of coating (Fig. 8: sample 4 shows two dark spots where the penetration occurred and much likely got clogged by corrosion products from the substrate). The OCP measurements of coatings are consistent with residual stress calculations. Indeed, coatings 1, 2, 3, 5 and 6 showed compressive residual stresses (Fig. 7) after polishing (superficial layer removed), whereas coating 4 showed tensile residual stresses. Certainly, compressive residual stresses are beneficial for corrosion applications because of their tendency to close any possible open path towards the substrate. After OCP measurements, the surfaces of coatings 2, 3 and 4 were analysed by grazing incidence X-ray diffractometry. Accordingly to GID patterns, neither localized nor generalized corrosion products were detected for coatings 2 and 3; instead, coating 4 showed 3 small intensity peaks (red circles in Fig. 9) attributed to iron oxyhydroxide FeO(OH) (JCPDS 98-024-5057), commonly known as the main component of rust when dealing with aqueous solutions.

3.2.2. Potentiodynamic polarization behaviour

The electrochemical behaviour of the coatings is shown in Fig. 10. The corrosion potential (E_{corr}), corrosion current density (i_{corr}), anodic (β_a) and cathodic (β_c) Tafel slopes and polarization resistance (R_p) obtained
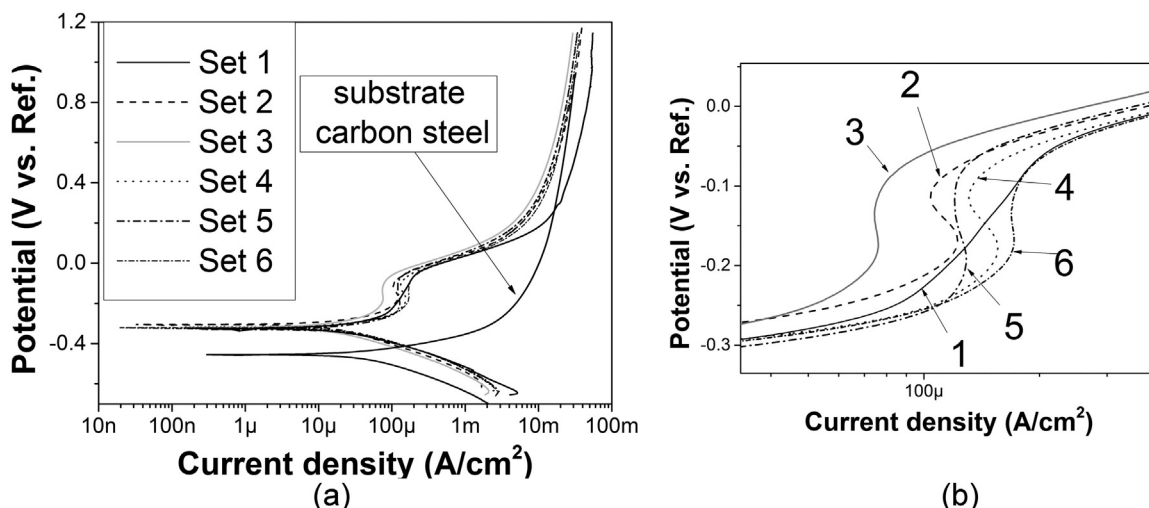

(a)

(b)

Fig. 10. a) Polarization behaviour of HVAF-sprayed coatings and substrate in HCl 0.1 M and b) magnification of pseudopassivation track of polarization measurement.

Table 5
Corrosion potential E_{corr}, corrosion current I_{corr}, anodic and cathodic Tafel lines slopes β_a, β_c and polarization resistance R_p of sprayed coatings.

Set	E_{corr} (mV)	i_{corr} ($\mu A/cm^2$)	β_a (mV/dec.)	β_c (mV/dec.)	R_p ($\Omega\ cm^2$)
1	−316	28.6	147	140	1086
2	−306	19.4	121	135	1435
3	−320	17.9	151	127	1675
4	−317	32.1	132	136	907
5	−328	34.7	149	128	863
6	−321	35.8	159	138	897

by potentiodynamic polarization technique are summarised in Table 5. The corrosion potential values of the coatings range from −300 mV to −328 mV, showing negligible differences between the various samples. As shown in Fig. 10(a) the polarization curves of the coatings are shifted towards more noble values of potential and lower current density compared to that of carbon steel substrate proving better protection in chlorine environment. In addition, the presence of pseudo-passivation behaviour during anodic polarization at current densities of 100 μA/cm² (Fig. 10(b)) was detected for all sprayed coatings. The current density of 3 sample is lower compared to that of all the other tested coatings, which is much likely due the formation of a more stable and protective superficial layer. The largest pseudo-passivation current densities are reported for samples 4, 5 and 6.

Regarding the polarization resistance calculated in Table 5, the largest R_p was consistently reported for sample 3 ($1.64°10^3\ \Omega\ cm^2$) due to the low current density and relatively high Tafel slopes. Indeed, high Tafel slopes lead to lower anodic and cathodic current at the same overpotential during the polarization measurements which in turn results in higher polarization resistance as depicted by Eq. (6). Consistent with OCP measurements and with open porosity estimations by EIS, sample 4 showed the lowest polarization resistance (832 Ω cm²) and the highest corrosion current density (more than twice as high as that of sample 3), much likely due to the high porosity and, therefore, to the large electrode/electrolyte interface or interconnected porosity through the coating towards the substrate. This proves the fundamental importance of limiting any kind of electrolyte paths for assuring higher corrosion protection.

4. Conclusions

The aim of this study was to evaluate the effect of HVAF process parameters on the microstructural and corrosion properties of Fe-based coatings. This kind of materials can be exploited for their low price, reduced health hazardousness, and for their good mechanical properties, and they can represent future alternative solutions in demanding corrosion and wear applications. Six sets of spray parameters were chosen by varying the combustion gas pressures and by selecting two different powder feeding rates. The main conclusions are listed as follows:

- HVAF Fe-based coatings showed dense microstructure with negligible porosity (SEM analysis). Some pores were detected in the outer layer of the coatings due to the intrinsic lack of hammering effect during subsequent particle impacts. Minor changes in crystalline phases from powder to coatings were reported. All coatings showed broadened X-ray diffraction peaks of austenite in comparison to the powder, due to micro-strains and/or to grain refinement, which in turn is most likely due to high particle deformation and rapid quenching. According to cross-sectional SEM/EDS analysis and XRD phase-evaluation large amount of chromium and iron mixed boride $(Cr,Fe)_2B$ was present in coatings. Few oxide inclusions were found in the coatings.
- Electrochemical impedance spectroscopy (EIS) allowed a quantitative, though indirect estimation of the open porosity according to the values of double layer capacitance and charge transfer resistance at the electrolyte/working electrode interface. One parameter setting, characterised by low powder feed rate (75 g/min) and by average air pressure/propane pressure ratio (116/106), emerged as the one (sample 3) exhibiting the lowest open porosity.
- The same sample (3) was also reported to possess the highest compressive residual stresses, with beneficial effects on corrosion and polarization resistance. Under these deposition conditions, the limited heat input from the flame and the higher flame velocity brought to higher particle deformation without worsening the overall powder softening and so the particle deposition.
- Fig. 11 summarises all of the present results by showing the correlation between residual stresses, charge transfer resistance from EIS tests (estimation of open porosity), and polarization resistance (measuring the electrochemical corrosion resistance in 0.1 M HCl) for all samples. The performances of the best and worst sample, deposited with the same air pressure/propane pressure ratio (116/106) but with low and high powder feed rates (respectively), are particularly highlighted in the figure. The combination of high compressive residual stress and high charge transfer resistance (low open porosity) resulted beneficial for the polarization resistance.

References

[1] L. Pawlowski, The Science and Engineering of Thermal Spray Coatings. 2nd edition, John Wiley & Sons, Chichester, West Sussex, 2008. 67–165.

[2] R.Q. Guo, C. Zhang, Y. Yang, Y. Peng, L. Liu, Corrosion and wear resistance of a Fe-based amorphous coating in underground environment, Intermetallics 30 (2012) 94–99.

[3] R.Q. Guo, C. Zhang, Q. Chen, Y. Yang, N. Li, L. Liu, Study of structure and corrosion resistance of Fe-based amorphous coatings prepared by HVAF and HVOF, Corros. Sci. 53 (2011) 2351–2356.

[4] Z. Zeng, N. Sakoda, T. Tajiri, S. Kuroda, Structure and corrosion behavior of 316 L stainless steel coatings formed by HVAF spraying with and without sealing, Surf. Coat. Technol. 203 (2008) 284–290.

[5] S. Bose, High Temperatures Coatings. , Elsevier Inc., Burlington, USA, 2007. 33–52.

[6] H. Hériaud-Kraemer, G. Montavon, S. Hertert, H. Robin, C. Coddet, Harmful risks for workers in thermal spraying: a review completed by a survey in a French company, J. Therm. Spray Technol. 12 (4) (2003) 542–554.
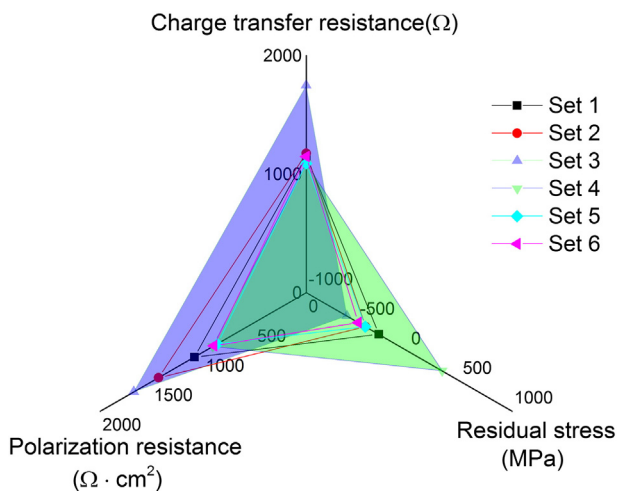
Fig. 11. Radar diagram of HVAF-sprayed Fe-based coatings. Filled areas correspond to sample 3 (violet) and sample 4 (green). (For interpretation of the references to color in this figure legend, the reader is referred to the web version of this article.)

[7] U.S. Department of Health, Human Services, Cobalt–tungsten carbide: powders and hard metals, 12th Report on CarcinogensJune 10, 2011.
[8] M.F. Morksa, Y. Tsunekawab, M. Okumiyab, Characterization and properties of splats sprayed with different cast iron powders, Mater. Lett. 58 (2004) 2481–2485.
[9] K. Volenik, F. Hanousek, P. Chraska, J. Ilavsky, K. Neufuss, In-flight oxidation of high-alloy steels during plasma spraying, Mater. Sci. Eng. A272 (1999) 199–206.
[10] A. Edrisy, T. Perry, Y.T. Chengb, A.T. Alpas, Wear of thermal spray deposited low carbon steel coatings on aluminum alloys, Wear 251 (2001) 1023–1033.
[11] O. Redjdala, B. Zaidb, M.S. Tabtic, K. Hendad, P.C. Lacazee, Characterization of thermal flame sprayed coatings prepared from FeCr mechanically milled powder, Int. J. Mater. Prod. Technol. 213 (2013) 779–790.
[12] B. Wielage, H. Pokhmurska, M. Student, V. Gvozdeckii, T. Stupnyckyj, V. Pokhmurskii, Iron-based coatings arc-sprayed with cored wires for applications at elevated temperatures, Surf. Coat. Technol. 220 (2013) 27–35.
[13] F. Bin-you, H. Ding-yong, Z. Li-dong, Effect of heat treatment on the microstructure and mechanical properties of Fe-based amorphous coatings, J. Alloys Compd. 480 (2009) 422–427.
[14] Z. Zhou, L. Wang, F.C. Wang, H.F. Zhang, Y.B. Liu, S.H. Xu, Formation and corrosion behavior of Fe-based amorphous metallic coatings by HVOF thermal spraying, Surf. Coat. Technol. 204 (2009) 563–570.
[15] B. Rajasekaran, G. Mauer, R. Vaßen, A. Röttger, S. Weber, W. Theisen, Development of cold work tool steel based-MMC coating using HVOF spraying and its HIP densification behaviour, Surf. Coat. Technol. 204 (2010) 3858–3863.
[16] G. Bolelli, B. Bonferroni, J. Laurila, L. Lusvarghi, A. Milanti, K. Niemi, P. Vuoristo, Micromechanical properties and sliding wear behaviour of HVOF-sprayed Fe-based alloy coatings, Wear 276–277 (2012) 29–47.
[17] Z.B. Zheng, Y.G. Zheng, W.H. Sun, J.Q. Wang, Erosion–corrosion of HVOF-sprayed Fe-based amorphous metallic coating under impingement by a sand-containing NaCl solution, Corros. Sci. 76 (2013) 337–347.
[18] M. Hasan, J. Stokes, L. Looney, M.S.J. Hashmi, Effect of spray parameters on residual stress build-up of HVOF sprayed aluminium/tool-steel functionally graded coatings, Surf. Coat. Technol. 202 (2008) 4006–4010.
[19] Y.Y. Santana, J.G. La Barbera-Sosa, M.H. Staia, J. Lesage, E.S. Puchi-Cabrera, D. Chicot, E. Bemporad, Measurement of residual stress in thermal spray coatings by the incremental hole drilling method, Surf. Coat. Technol. 201 (2006) 2092–2098.
[20] J.M. Guilemany, J. Fernandeza, N. Espallargas, P.H. Suegama, A.V. Benedetti, Influence of spraying parameters on the electrochemical behaviour of HVOF thermally sprayed stainless steel coatings in 3.4% NaCl, Surf. Coat. Technol. 200 (2006) 3064–3072.
[21] S. Liu, D. Sun, Z. Fan, H.Y. Yu, H.M. Meng, The influence of HVAF powder feedstock characteristics on the sliding wear behaviour of WC–NiCr coatings, Surf. Coat. Technol. 202 (2008) 4893–4900.
[22] Q. Wang, S. Zhang, Y. Cheng, J. Xiang, X. Zhao, G. Yang, Wear and corrosion performance of WC–10Co4Cr coatings deposited by different HVOF and HVAF spraying processes, Surf. Coat. Technol. 218 (2013) 127–136.
[23] A. Verstak, V. Baranovski, Deposition of carbides by activated combustion HVAF spraying, Thermal Spray 2004 — Advances in Technology and Application — Proceedings of the International Thermal Spray Conference 2004, ASM International, Materials Park, OH, USA 2004, pp. 551–555.
[24] L.-M. Berger, R. Puschmann, J. Spatzier, S. Matthews, Potential of HVAF spray processes, Therm. Spray Bull. 6 (1) (2013) 16–20.
[25] A. Milanti, H. Koivuluoto, P. Vuoristo, Influence of the spray gun type on microstructure and properties of HVAF-sprayed Fe-based novel corrosion resistant coatings, Thermal Spray 2014: Not Fiction: Thermal Spray the Key Technology in Modern Life!May 21–23, 2014. (Barcelona, Spain, 6 pp.).
[26] A.P. Wang, Z.M. Wang, J. Zhang, J.Q. Wang, Deposition of HVAF-sprayed Ni-based amorphous metallic coatings, J. Alloys Compd. 440 (2007) 225–228.
[27] S.L. Liu, X.P. Zheng, G.Q. Geng, Influence of nano-WC–12Co powder addition in WC–10Co–4Cr AC-HVAF sprayed coatings on wear and erosion behavior, Wear 269 (2010) 362–367.
[28] K. Tao, X.L. Zhou, H. Cui, J.S. Zhang, Oxidation and hot corrosion behaviors of HVAF-sprayed conventional and nanostructured NiCrC coatings, T. Nonferr. Metal. Soc. 19 (2009) 1151–1160.
[29] I. Hulka, V.A. Şerban, I. Secoşan, P. Vuoristo, K. Niemi, Wear properties of CrC–37WC–18M coatings deposited by HVOF and HVAF spraying processes, Surf. Coat. Technol. 210 (2012) 15–20.
[30] C. Lyphout, K. Sato, Screening design of hard metal feedstock powders for supersonic air fuel processing, Surf. Coat. Technol. 258 (2014) 447–457.
[31] P. Vuoristo, S. Ahmaniemi, S. Tuurna, T. Mäntylä, E. Cordano, F. Fignino, G.C. Gualco, Development of HVOF sprayed NiCoCrAlYRe coatings for use as bond coats of plasma sprayed thermal barrier coatings, International Thermal Spray Conference, 6 2002, pp. 470–475.
[32] G. Bolelli, I. Hulka, H. Koivuluoto, L. Lusvarghi, A. Milanti, K. Niemi, P. Vuoristo, Properties of WC–FeCrAl coatings manufactured by different high velocity thermal spray processes, Surf. Coat. Technol. 247 (2014) 74–89.
[33] B. Eigenmann, E. Macherauch, Röntgenographische Untersuchung von Spannungszuständen in Werkstoffen, Mater. Werkst. 27 (1996) 426–437.
[34] D.A. Jones, Principle and Prevention of Corrosion., Macmillan Pub. Co, 1991. 568.
[35] G. Antou, G. Montavon, F. Hlawka, A. Cornet, C. Coddet, Exploring thermal spray gray alumina coating pore network architecture by combining stereological protocols and Impedance Electrochemical Spectroscopy, J. Therm. Spray Technol. 15 (2006) 765–772.
[36] J. Zhang, V. Desai, Evaluation of thickness porosity and pore shape of plasma sprayed TBC by Electrochemical Impedance Spectroscopy, Surf. Coat. Technol. 190 (2005) 98–109.
[37] G. Bolelli, V. Cannillo, R. Gadow, A. Killinger, L. Lusvarghi, J. Rauch, Properties of high velocity suspension flame sprayed (HVSFS) TiO₂ coatings, Surf. Coat. Technol. 203 (2009) 1722–1732.
[38] S. Kuroda, M. Watanabe, K. Kim, H. Katanoda, Current status and future prospects of warm spray technology, J. Therm. Spray Technol. 20-4 (2011) 653–676.
[39] A.P. Wang, Z.M. Wang, J. Zhag, J.Q. Wang, Deposition of HVAF-sprayed Ni-based amorphous metallic coatings, J. Alloys Compd. 440 (2007) 225–228.
[40] G.J. Brug, A.L.G. Van Den Eeden, M. Sluyters-Rehbach, J.H. Sluyters, The analysis of electrode impedances complicated by the presence of a constant phase element, J. Electroanal. Chem. 176 (1984) 275–295.
[41] B. Hirschorn, M.E. Orazem, B. Tribollet, V. Vivier, I. Frateur, M. Musiani, Determination of effective capacitance and film thickness from constant-phase-element parameters, Electrochim. Acta 55 (2010) 6218–6227.
[42] http://henke.lbl.gov/optical_constants/atten2.html (last accessed 17/02/2015).